ADVANCED ELECTRONIC MATERIALS Open Access
www.advelectronicmat.de

Impact of Non-Stoichiometric Phases and Grain Boundaries on the Nanoscale Forming and Switching of HfO_x Thin Films

*Niclas Schmidt, Nico Kaiser, Tobias Vogel, Eszter Piros, Silvia Karthäuser, Rainer Waser, Lambert Alff, and Regina Dittmann**

HfO_2 is one of the most common memristive materials and it is widely accepted that oxygen vacancies are prerequisite to reduce the forming voltage of the respective memristive devices. Here, a series of six oxygen engineered substoichiometric HfO_{2-x} thin films with varying oxygen deficiency is investigated by conductive atomic force microscopy (c-AFM) and the switching process of substoichiometric films is observed on the nanoscale. X-ray diffractometry (XRD) exhibits a phase transition from stoichiometric, monoclinic HfO_2 toward oxygen deficient, rhombohedral $HfO_{1.7}$. The conductance of HfO_{2-x} is increasing with increasing oxygen deficiency, which is consistent with the increasing prevalence of the highly conductive rhombohedral phase. Simultaneously, c-AFM reveals significant local conductivity differences between grains and grain boundaries, regardless of the level of oxygen deficiency. Single grains of highly oxygen deficient samples are formed at significant lower voltages. The mean forming voltage is reduced from (7.0 ± 0.6) V for HfO_2 to (1.9 ± 0.8) V for $HfO_{1.7}$. Resistive switching on the nanoscale is established for single grains for the highest deficient thin film samples. The final resistance state is thereby dependent on the initial conductivity of the grains. These studies offer valuable insights into the switching behavior of memristive polycrystalline HfO_2.

1. Introduction

Hafnium oxide is widely used in valence change mechanism (VCM) type of resistive random-access memories (ReRAM).[1–3] Since the underlying switching mechanism is based on the movement of oxygen vacancies, the oxygen concentration of HfO_2 in the virgin state, as well as within the filaments after electroforming is of key relevance for the performance of HfO_2-based devices. Investigations on oxygen deficient HfO_{2-x} and the impact of resulting substoichiometric phases on the electronic and in particular resistive switching properties are rare.[4,5]

The introduction of oxygen vacancies or other defects is one way to influence the structure and the electronic properties, such as the band structure or conductivity.[6–9] Both, doping with foreign atoms and introducing oxygen vacancies, has strong impact on the stability of the different HfO_2 phases in the rich phase diagram.[10–12] Defects have furthermore a vigorous effect onto the resistive switching characteristics.[13–15] The formation of conductive filaments is attributed to the release of oxygen from the HfO_2 lattice and the movement of oxygen vacancies, resulting in the highest level of oxygen deficiency in the local filament region.[16–19] An existing oxygen deficiency in the virgin films is proven to lower the forming voltage.[20] For HfO_{2-x}, the range of oxygen deficiency for the most efficient forming process was calculated to be within $HfO_{1.50}$ to $HfO_{1.75}$.[21] For a certain level of oxygen deficiency even forming-free resistive switching is possible.[22,23]

N. Schmidt, S. Karthäuser, R. Waser, R. Dittmann
Peter Grünberg Institute (PGI-7) and JARA-FIT
Forschungszentrum Jülich GmbH
52425 Jülich, Germany
E-mail: r.dittmann@fz-juelich.de

The ORCID identification number(s) for the author(s) of this article can be found under https://doi.org/10.1002/aelm.202300693

DOI: 10.1002/aelm.202300693

N. Schmidt
Faculty 1 - Mathematics
Computer Science and Natural Science
RWTH Aachen University
52062 Aachen, Germany

N. Kaiser, T. Vogel, E. Piros, L. Alff
Advanced Thin Film Technology Division
Institute of Materials Science
TU Darmstadt
64287 Darmstadt, Germany

R. Waser
Institute of Materials in Electrical Engineering and Information Technology (IWE 2)
RWTH Aachen University
52056 Aachen, Germany

Additionally to the presence of oxygen vacancy point defects, the significance of grain boundaries for the formation of conductive pathways in polycrystalline HfO_2 was repeatedly demonstrated.[24–26] Hence, grain boundaries are preferred locations for resistive switching,[27–29] and it was proven that the forming voltage can be purposefully tuned by grain boundary engineering.[5,30]

In order to gain insights into the impact of substoichiometric phases and grain boundaries on forming and switching of HfO_2 thin film devices, c-AFM is an ideal tool. It has been utilized to investigate resistive switching with spatial resolution,[31–37] or to probe the previously formed conductive filament with diameter as small as about 3 nm after removal of the top electrode.[38,39] While previous studies investigated the switching for stoichiometric hafnium oxide,[27,28] there exist no spatially resolved investigations of the switching properties for oxygen deficient samples in order to address the impact of substoichiometric phases on the nanoscale. In addition, the direct observation of the forming process or the resistive switching of distinct parts of a single grain by c-AFM is missing, although this is highly relevant for the question of ultimate device scaling.

In our previous work we have shown that HfO_{2-x} thin films can be grown with a precise adjustment of their oxygen deficiency by molecular beam epitaxy (MBE).[4,6,40] The oxygen vacancy density and the phases are determined by the Hf/O-ratio during growth. In particular, Kaiser et al.[40] demonstrated phase transitions, from monoclinic *m*-HfO_2 to rhombohedral *r*-$HfO_{1.7}$ and with further oxygen reduction even to hexagonal *h*-$HfO_{0.7}$, quantified via in vacuo X-ray photoelectron spectroscopy. The pseudocubic phase of $HfO_{1.7}$ was first analyzed by comprehensive XRD analysis by Kaiser et al.[6] and through collaborative experimental and theoretical efforts the rhombohedral nature (*r*-HfO_{2-x}) was pinpointed.[40] The phase transitions were accompanied by a strong decrease in resistance.[6]

Here, we aim to study the electric properties of HfO_{2-x} thin films with respect to the grown phases and for an accurately specified oxygen deficiency, by using a well defined set of thin film samples. In detail, we investigate the electrical and resistive switching properties of this model system of oxygen engineered thin films by c-AFM. We explore the elementary resistive switching properties of the model system, with a specific focus on surface characteristics. It is important to note that the resistive switching behavior in devices based on oxygen deficient thin films may differ due to differences in the electrode geometry, the field distribution and the thermal environment. Thus, the influence of the HfO_{2-x} phases and of the grain boundaries on the conductivity, as well as on the forming voltage of single HfO_{2-x} grains is targeted. With the spatial resolution of c-AFM the growth of the conductive filament with the applied voltage is probed. Thereby, the filament formation is observed directly at the pristine surface with respect to local surface features, like grain boundaries and grain height. This method allows us to study the impact of oxygen deficiency on the resistive switching behavior of single grains on the nanoscale.

2. Results and Discussion

In order to investigate the nanostructure and local current transport characteristics in the vicinity of insulating to conducting hafnium oxide, HfO_{2-x}/TiN/Al_2O_3 stacks with varying oxygen content in the HfO_{2-x} layer were fabricated.[40] TiN was chosen as bottom electrode, as depicted in **Figure 1a**, since this material is commonly used in complementary metal-oxide-semiconductor (CMOS) technology and known in ReRAM research.[41] The epitaxial TiN was grown with a layer thickness of 34 nm onto c-cut Al_2O_3 substrates and has a roughness of RMS = 0.59 nm (measured on 500 nm by 500 nm image in

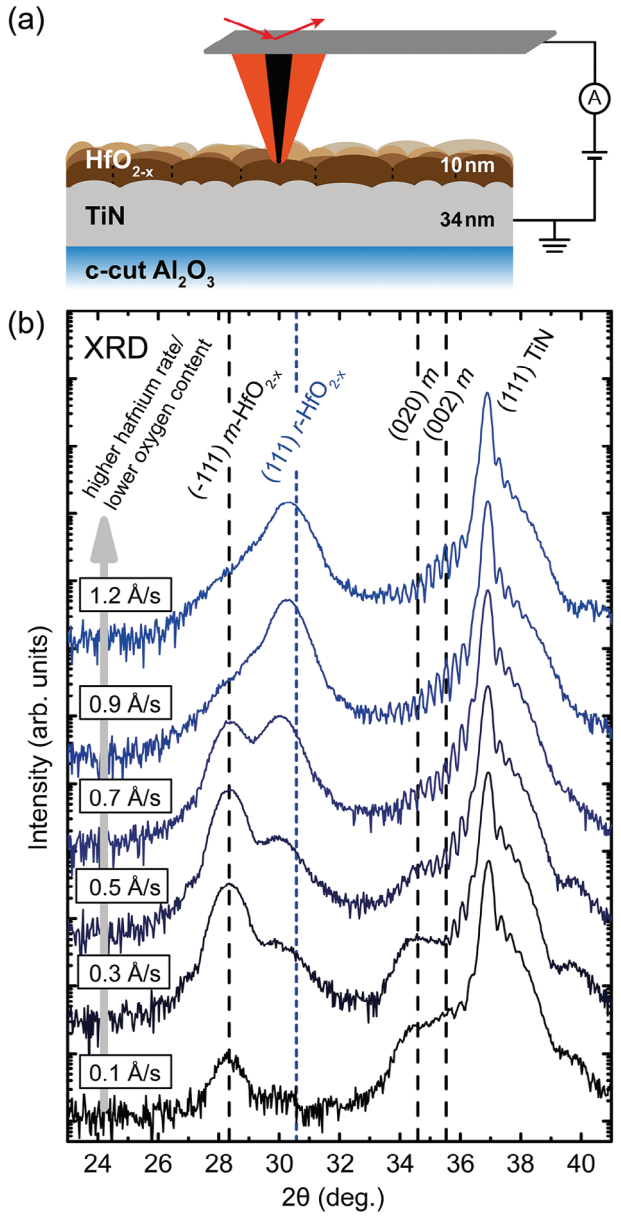

Figure 1. a) Investigated HfO_{2-x}/TiN/Al_2O_3 stack configuration and indicated c-AFM measurement setup (orange: PtIr-cantilever; black: single crystal diamond cantilever). Epitaxial TiN, which is grown on c-cut Al_2O_3, serves as bottom electrode. b) $2\theta/\omega$ XRD measurements show the phase transition from *m*-HfO_2 to oxygen vacancy stabilized *r*-$HfO_{1.7}$ by changing the hafnium rate, while maintaining constant oxygen flow and plasma energy during MBE deposition. The Laue oscillations of the TiN layer indicate high quality epitaxial film growth through highly coherent lattice planes.

Figure S2, Supporting Information), which allows for the synthesis of HfO_{2-x} films of low roughness, as well. For details of the TiN synthesis, see Experimental Section 4. For exclusion of the influence of oxidation effects, all samples were kept in vacuum from MBE synthesis throughout c-AFM analysis (for details, see Section 4).

In Figure 1b the $2\theta/\omega$ XRD measurements of the $HfO_{2-x}/TiN/Al_2O_3$ sample series illustrate the phase transition from stoichiometric, monoclinic to oxygen vacancy stabilized, rhombohedral hafnium oxide. In order to access a broad range of oxidation conditions, the hafnium evaporation rate was varied from 0.1 to 1.2 Ås^{-1}, while maintaining a constant oxygen flow of 0.18 sccm. At ambient pressure and temperature stoichiometric hafnium oxide is of monoclinic structure.[42] As expected this is the predominant phase for the highest oxidation conditions at a Hf rate of 0.1 Ås^{-1} with visible reflexes of (−111), (020), and (002) (compare PDF 00-034-0104). When reducing the oxygen content by increasing the hafnium rate, the monoclinic (-111) *m* orientation first becomes more dominant as compared to the (020) *m* and (002) *m* orientations, but gradually all monoclinic reflections vanish. At the same time, the appearance of a second hafnium oxide phase becomes evident through the (111) *r*-HfO_{2-x} reflection.

The phase transition from monoclinic to rhombohedral hafnium oxide on TiN closely resembles the observed phase transition from discussed previous works, where hafnium oxide was directly deposited on c-cut Al_2O_3.[40] As suggested by density-functional theory calculations, this phase transition is mainly driven by oxygen substoichiometry.[40] In our previous studies,[6,40] the stoichiometry of the sample with the highest amount of rhombohedral phase in Figure 1b is determined as $HfO_{1.7}$. For further information on the oxygen content of substoichiometric monoclinic-rhombohedral, or even rhombohedral-hexagonal phase mixtures, we refer to our previous work dealing with the systematic investigation of the full range of oxygen stoichiometry from monoclinic to hexagonal hafnium oxide.[6,40] This series of $HfO_{2-x}/TiN/Al_2O_3$ thin film samples was specially designed for the following investigations, since the aforementioned studies clearly correlate the stoichiometry and electrical properties of identified *r*-$HfO_{1.7}$, highlighting a transition from insulating to conducting behavior.

The oxygen content in the grown HfO_{2-x} thin films is exclusively adjusted by the Hf growth rate in the MBE. For simplicity, the samples are hereinafter denominated with the corresponding Hf rate in parentheses, e.g., Hf(0.1) for a rate of 0.1 Ås^{-1}. According to a previous investigation by Kaiser et al.[40] and the XRD data in Figure 1b the sample series ranges from *m*-HfO_2 for Hf(0.1) to *r*-$HfO_{1.7}$ for Hf(1.2).

All six samples were investigated by c-AFM. An exemplary topography, acquired with the c-AFM PtIr-cantilever, is displayed in **Figure 2**a for sample Hf(0.9), including a height profile along the dashed line in Figure 2b. The topography of Hf(0.9) reveals a typical roughness of RMS = 0.89 nm and a mean grain diameter of around 26.0 nm. The surface roughness and mean grain diameter, assuming circular shaped grains, are summarized in Table S1 (Supporting Information) for all samples. The mean RMS value for exemplary scan areas of all samples (Hf(0.1) to Hf(1.2)) is (0.83 ± 0.12) nm. The diameter of a single grain is normally distributed around a mean value of (26.7 ± 1.0) nm.

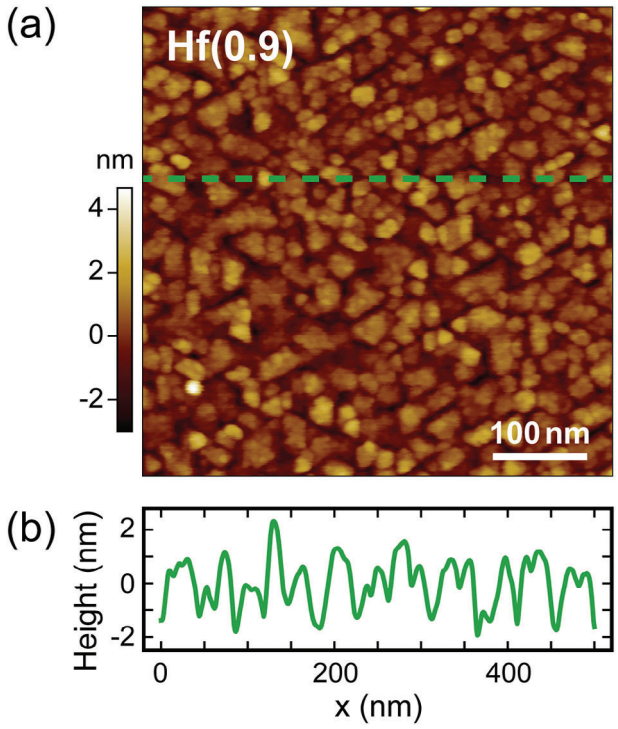

Figure 2. a) AFM topography of Hf(0.9), grown with a Hf rate of 0.9 Ås^{-1} and resulting RMS of 0.89 nm, measured over the entire image, exemplary for investigated HfO_{2-x} thin films. b) Height profile along the dashed line in (a).

This underlines that the 10 nm HfO_{2-x} layer consists of single grains over the entire film thickness. For further details about the topography of the samples see Chapter S3 (Supporting Information). For the RMS values, as well as the grain size no trend with changing Hf growth rate and the resulting stoichiometry can be determined. The topological appearance of the nanostructure remains unaffected by the clear phase change from *m*-HfO_2 to *r*-$HfO_{1.7}$, like presented in Figure 1.

As a next step, the electrical properties of the samples were thoroughly investigated with c-AFM. For Hf(1.2), which has the highest conductivity, an excerpt from the series is shown in **Figure 3**a–d. The initial topography and conductivity, Figure 3a,b, respectively, were measured with a SET voltage of V_{set} = 0.10 V. Here, only a few conductive spots with current below 2 nA were detected. Subsequently, the SET voltage was increased from 0.25 to 2.00 V in 0.25 V steps. The current maps for SET voltages of 1.25 and 2.00 V are displayed in Figure 3c,d, respectively. The complete set of current maps and the topography for the lowest and highest SET voltage is presented in Figure S4 (Supporting Information). The topography stays unchanged during the whole series. The current map in Figure 3c (V_{set} = 1.25 V) reveals multiple highly conductive spots with currents above the detection limit of 333 nA. For a voltage of 2.00 V in Figure 3d these conductive spots expand and additionally multiply to numerous more highly conductive areas. With another voltage increase to 2.25 V the whole scan area turns fully conductive and reaches the measurement limitation of the system, which inhibits a further stable c-AFM scan.

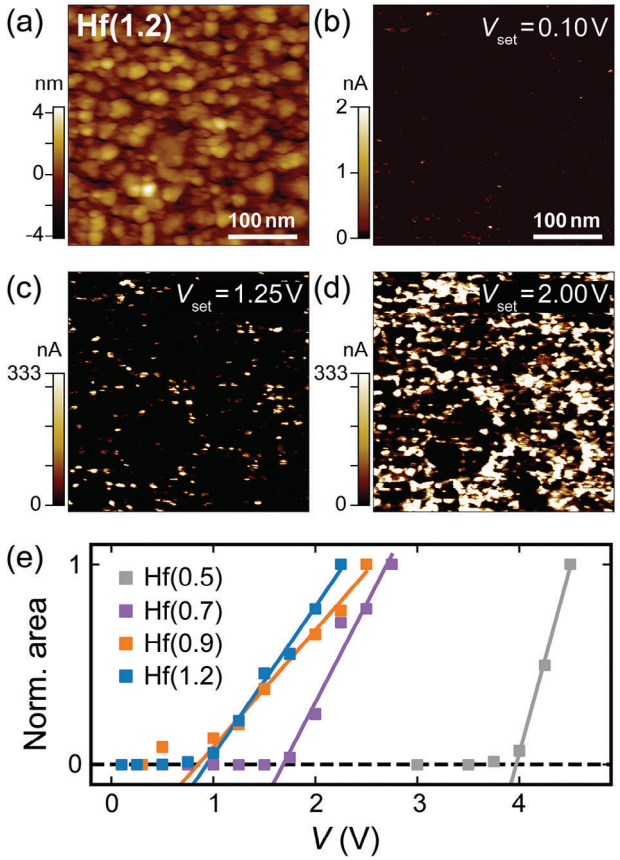

Figure 3. a) AFM topography with roughness of RMS = 0.95 nm and corresponding current maps for the same area with SET voltages of b) 0.10 V, c) 1.25 V, and d) 2.00 V for sample Hf(1.2), *r*-$HfO_{1.7}$. For all voltages no changes in topography are detected. e) Min-max normalized area with a current above 2 nA for oxygen deficient samples Hf(1.2) to Hf(0.5). The intersection of the fit with the black dashed baseline results in the voltage onset V_{onset}.

Analogous to Hf(1.2), voltage series were carried out on the samples Hf(0.9), Hf(0.7), and Hf(0.5). Conductive AFM mapping was not possible for the samples Hf(0.3) and Hf(0.1) since the weak conductivity required such high voltages (above ≈6 V), that led to instabilities during imaging. Acquired current maps were analyzed for the area with current above the threshold of 2 nA. The conductive area was subsequently min-max normalized relatively for each sample. For details about the normalization see Chapter S4 (Supporting Information). For the four most oxygen deficient samples the normalized area with respect to the SET voltage is plotted in Figure 3e. The intersection of the fit to the normalized conductive area with the black dashed baseline results in the voltage onset V_{onset}. Samples Hf(1.2) (blue) and Hf(0.9) (orange) behave similarly with V_{onset} of about 0.9 and 0.8 V, respectively. Sample Hf(0.7) (purple) has V_{onset} at ≈ 1.7 V, while V_{onset} of Hf(0.5) (grey) is significantly larger at about 4.0 V. The different V_{onset} demonstrate higher conductivity of the most deficient samples, while the conductivity is significantly less already for sample Hf(0.5).

A higher V_{onset} presumably means a higher resistivity of the HfO_{2-x} layer. It is proven that the resistivity of a monoclinic hafnium oxide layer can be lowered by increasing oxygen deficiency.[43] Here, the voltage onset can furthermore be correlated to the different phases detected in the XRD data in Figure 1b. The samples Hf(1.2) and Hf(0.9) have the highest conductivity and the XRD scans reveal, that for both samples the rhombohedral phase is clearly dominant. The conductivity of Hf(0.7) is already lowered and here the intensity of the peak of the monoclinic phase levels the peak of the rhombohedral phase. For sample Hf(0.5) the conductivity is considerably decreased with the intensity of the peak for the monoclinic phase already exceeding the intensity of the rhombohedral phase in Figure 1b. For Hf(0.3) and Hf(0.1), the conductivity is even lower which is attributed to the monoclinic phase, the solely found phase in stoichiometric HfO_2. Therefore, the higher conductivity is assigned to the increasing prevalence of the rhombohedral phase with increasing oxygen deficiency, which is in agreement with previous studies.[6]

The conductivity measured by c-AFM shows a strong dependence on the hafnium to oxygen ratio, and therefore confirms the strong influence of oxygen vacancies on the electrical properties. The trend in onset voltages, as displayed in Figure 3, clearly demonstrates the increasing electrical conductivity with decreasing oxygen content. Also, devices prepared in a metal-insulator-metal structure exhibit reduced forming voltages with increasing oxygen deficiency of the hafnium oxide layer.[4] Reduced forming voltages are usually associated with a less violent soft breakdown, which in turn effects narrower statistical distributions for characteristic switching parameters, as well as reduced device to device variability.[4] Note that oxygen vacancies have an influence on the noise magnitude as observed in Y_2O_3 based filamentary switching devices.[44] We expect a similar behavior for HfO_x based structures.

For a more detailed localization of the positions of rising currents, the current map is superimposed onto the corresponding topography (see Figures S5 and S6, Supporting Information for details) for different SET voltages. For Hf(1.2) extracts of the superimposed maps are shown in **Figure 4** for 0.75 to 2.00 V. Current is visualized above a threshold of 2 nA. Thus, using the high spatial resolution it is possible to precisely identify at which positions current is detected for V_{onset}. Focusing on Figure 4a,b, current arises first along the grain boundaries as marked by the arrows. The onset is gradual and the current for the lowest voltage is within the 2 to 50 nA range. With the increased voltage of 1.25 V in Figure 4c, the current at the marked grain boundaries rapidly increases to above 100 nA or even above 300 nA, respectively.

Previous investigations indicated the enhanced conductivity along grain boundaries for stoichiometric hafnia and it was described for polycrystalline hafnia that the oxygen vacancy density is increased at the grain boundaries. This causes an elevated leakage current induced by defect states within the bandgap.[27,45,46] Here, we demonstrate for a series of highly controlled oxygen deficient HfO_{2-x} samples how the conductivity evolves with the respectively applied voltage on single, pristine grains. Thereby, the discrimination between conductive grain boundaries and conductive grain areas was possible using high resolution c-AFM imaging, as shown in Figure 4. At voltages below 1.25 V, current is solely measured along the grain boundaries. With increasing voltage up to 2.00 V, the conductive area expands from the first spots further along the grain boundaries and the current along

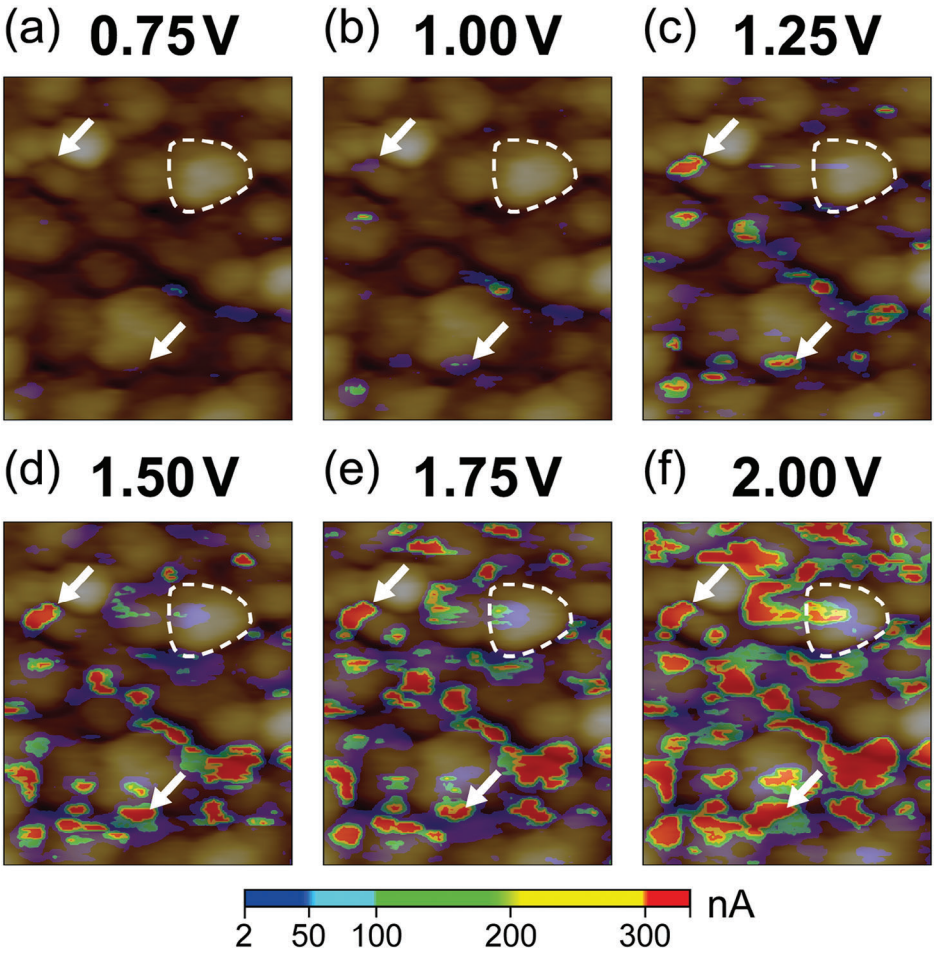

Figure 4. Current map superimposed onto c-AFM topography (see Figure S6, Supporting Information) for SET voltages of a) 0.75 V, b) 1.00 V, c) 1.25 V, d) 1.50 V, e) 1.75 V, and f) 2.00 V for sample Hf(1.2). Current is detected at first along the grain boundaries exemplary indicated by arrows. At higher voltage in (d), current is measured also through grains, as shown for the grain exemplary marked by the dashed line. With increasing voltage, current is increasing from positions, where it was already detected at lower bias, as marked by the arrows in (e) and (f). The current scale applies for (a–f). Current is visualized above 2 nA. The 100 nm by 120 nm scan area is an excerpt from Figure S5 (Supporting Information).

nearly all grain boundaries exceeds the current limitation of the scanning probe microscopy (SPM) system.

Starting at a minimum of 1.25 V and in particular at 1.50 V current is additionally measured through the first *r*-$HfO_{1.7}$ grains, as exemplary demonstrated for the marked grain in Figure 4. In Figure 4c, the current on the marked grain slowly evolves at the highest point of the grain and at 1.50 V in Figure 4d, the conductive area expands further in the middle of the grain. The same area reveals enhanced current for the next higher voltages in Figure 4e,f. At 2.00 V, current is acquired across the grain toward the grain boundary on the lower right side. However, not the entire grain is conductive and the current varies even within this single grain, indicating once again local variability of the oxygen vacancy density.

The leakage current remains higher for grain boundaries compared to the center of the grains regardless of the level of oxygen deficiency and the dominant phases. Tip-sample convolution can be excluded since at lower voltages, for example at 1.25 V, only selected grain boundaries have higher conductivity and current is measured centrally on grains, which are larger than the cantilever tip. The observations in Figure 4 are confirmed by c-AFM measurement with the single crystal diamond cantilever, see Figure S7 (Supporting Information) for details. The full series of current maps superimposed onto the topography for Hf(1.2) is displayed in Figure S5 (Supporting Information).

Since the conductivity of the samples, in particular at the grain boundaries, scales with the oxygen deficiency, as shown in Figure 3e, the forming voltage of the grains and its dependence on the phases was investigated and is presented in **Figure 5**. In order to examine the forming voltages, the cantilever tip was positioned centrally on a grain and *I–V* curves were performed thereupon. The feedback loop is switched off during the voltage sweep and unwanted oscillations of the used PtIr-cantilever due to excessive forces by extremely high biases are thus inhibited. Hence, spectroscopy was possible even toward the bias limitation of the system in contrast to imaging with high voltages above ≈6 V before. An example of a typical forming process is outlined for Hf(1.2) in Figure 5a. The position of the cantilever tip during the acquisition of the *I–V* curve is marked in the topography for the corresponding grain in the inset (blue dot). The grain

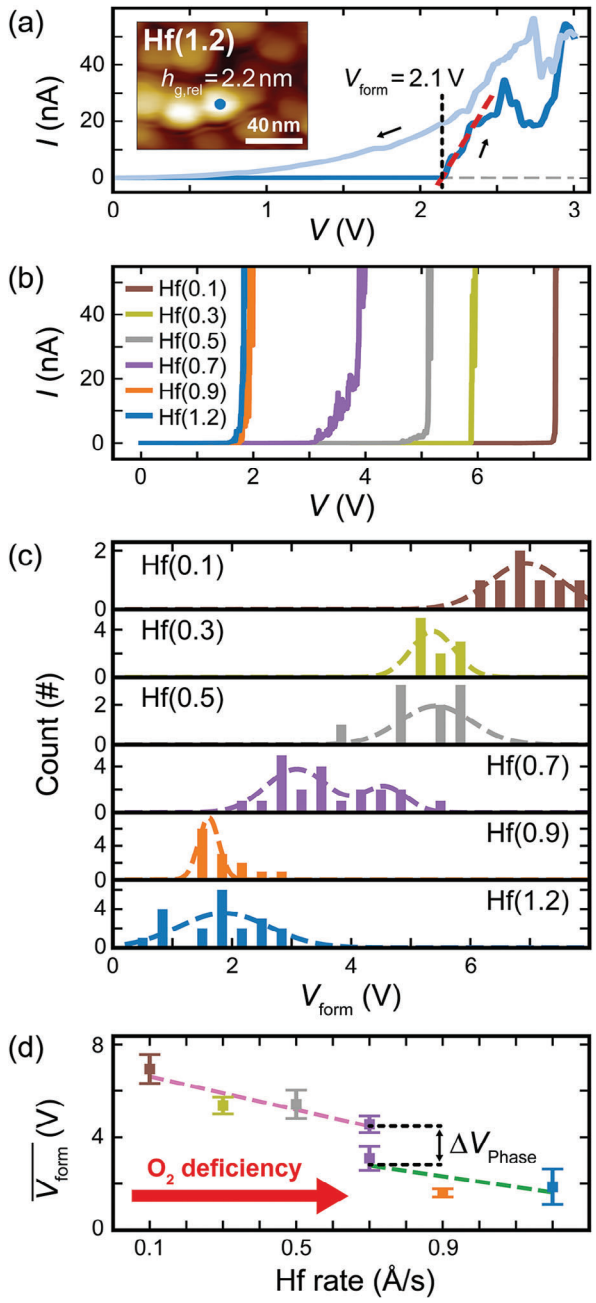

Figure 5. Forming voltage of single grains. a) Exemplary *I*–*V* curve during forming process on marked grain in AFM topography of Hf(1.2) (inset). Intersection of zero current baseline (grey) and fit to the blue forward current curve (red line) results in forming voltage V_{form}. Backward curve (light blue) with enhanced conductivity after forming. b) Exemplary *I*–*V* curves for fitting V_{form}, c) distribution of V_{form}, and d) mean V_{form} with respect to the Hf growth rate for all HfO_{2-x} samples including fit to *m*- (pink) and *r*-HfO_{2-x} (green).

has a relative height of $h_{g,\,rel}$ = 2.2 nm. For the *I*–*V* curves, the voltage was increased from zero bias until a significant current onset above 2 nA was detected like shown for the forward curve (blue) in Figure 5a. As a result of the forming process the current curve in backward direction (light blue) exhibits an enhanced conductivity. The intersection of the fit to the current onset and the zero current baseline results herein in a forming voltage of V_{form} = 2.1 V for the marked grain in the inset of Figure 5a. For all investigated samples the forming voltages were determined analogously.

Because of a certain variability in the height of the grains, the forming voltages were evaluated for a broad range of grain heights. The forming voltage with respect to the grain height is plotted in Figure S8 (Supporting Information) for all samples Hf(1.2) to Hf(0.1). No trend or dependence of V_{form} from the grain height can be derived. The variation in the grain height and the resulting differences of the electric field within the grain do not influence the forming noticeably. With the mean grain size of around 27 nm the forming through the HfO_{2-x} layer can be safely assumed to occur only within one single grain.

Exemplary forming curves, which were used for the evaluation of V_{form}, for grains of all six samples are presented in Figure 5b. The distribution of the forming voltage with a Gaussian fit for each sample is shown in Figure 5c. The forming voltages of the two most deficient samples Hf(1.2) and Hf(0.9) are normally distributed around the lowest values of 1.9 and 1.6 V, respectively. These two samples have grains of rhombohedral phase proven by the XRD scans in Figure 1b. The forming voltage of the stoichiometric, solely monoclinic sample Hf(0.1) is distributed around the highest value of 7.0 V. V_{form} is lowered for increasing oxygen deficiency for samples Hf(0.3) and Hf(0.5) to the same value of 5.4 V. Both samples reveal a dominating monoclinic peak in the XRD scan in Figure 1b. However, the forming voltage of grains of sample Hf(0.7) exhibits a binormal distribution in Figure 5c with peaks at 3.1 and 4.6 V. The XRD scan, compare Figure 1b, suggests a clear mixture of the monoclinic and rhombohedral phase fractions in Hf(0.7), as the (-111) monoclinic and (111) rhombohedral reflections are virtually identical in intensity. The binormal distribution of V_{form} indicates that single grains consist of rather one of the phases than a mixture of both.

The mean values of V_{form} according to the distribution in Figure 5c are shown with respect to the growth rate in Figure 5d. The pink and green dashed lines represent the fit to the forming voltages of grains of monoclinic and rhombohedral phase, respectively. Overall, the forming voltage is continuously decreasing with increasing oxygen deficiency indicated by both fit lines. Although the local acquisition of the forming voltage by c-AFM differs from real devices, the impact of oxygen deficiency on the forming voltage aligns well with findings from other studies on ReRAM device structures.[20,22] However, there is an additional voltage difference ΔV_{Phase} attributed to the phase transition between the monoclinic and the rhombohedral phase, which is outlined by the offset between the two fit lines in Figure 5d. At Hf(0.7), the sample with the same intensity for both phases in the XRD scan, the forming voltage of *r*-HfO_{2-x} grains is about 1.7 V smaller than of *m*-HfO_{2-x} grains.

The conductivity and the forming voltage of studied HfO_{2-x} grains and grain boundaries, Figures 3e and 5d, respectively, exhibit dependencies on the level of oxygen deficiency. Hence, also the resistive switching behavior was explored for samples with different oxygen defect density. The approach was thereby analogous to common methods of resistive switching via scanning probe techniques, as demonstrated in previous investigations.[33,35,47] The initial and present resistance state of

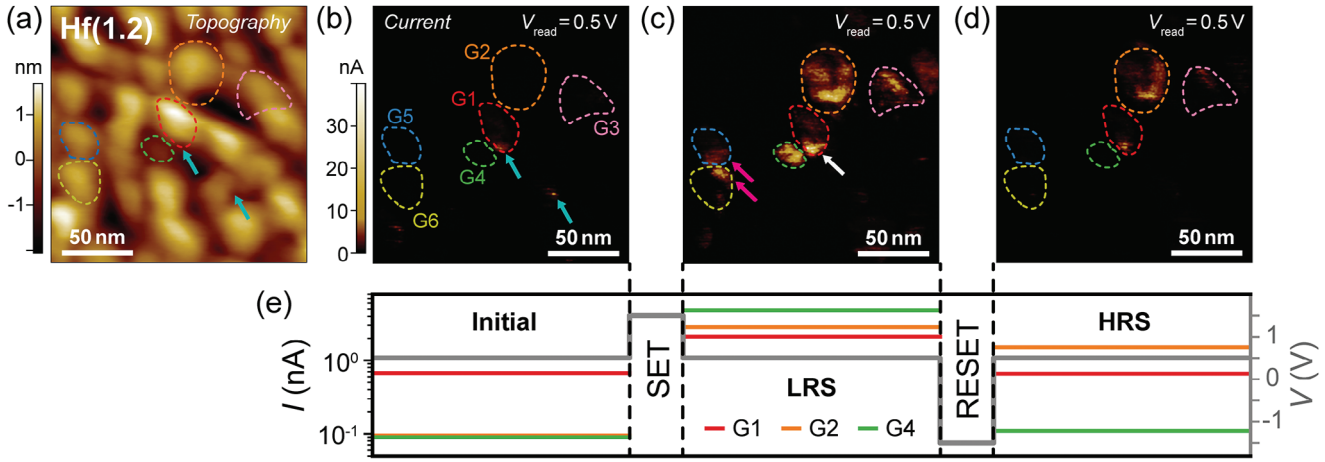

Figure 6. Resistive switching of single grains. All images are taken at the same position. Exemplary marked grains G1 to G6 as guide to the eye. a) AFM topography on Hf(1.2). b) Corresponding current map of initial conductivity state with singular occurring currents (blue arrows) acquired with readout voltage of V_{read} = 0.5 V. The current scale applies for (b–d). c) Readout of current map after switching with voltage of 1.5 V. All marked grains exhibit enhanced conductivity and therefore switching into the LRS. Highest currents detected at the grain boundaries (white and pink arrows). d) Current map during readout after scanning with −1.5 V in order to switch back into a high resistive state. Grains G1 to G3 show partially reduced conductivity, while grains G4 to G6 completely switch into the HRS. e) Left axis: Mean current of grains G1, G2, and G4 for (b–d). Right axis: Applied voltage (grey).

the surface area is read out with low voltages, while the scan area is switched with high voltages.

For Hf(1.2) an exemplary resistive switching process for single grains is demonstrated in **Figure 6**. The topography in Figure 6a stays unchanged during the whole switching process. The current maps in Figure 6b–d show the initial state, the low resistive state (LRS) and the high resistive state (HRS), respectively. The mean current for a selection of exemplary marked grains and the applied voltage is presented in Figure 6e, whereby the grains G1 to G3, as well as the grains G4 to G6 behave similarly.

At first, the topography and the grains initial resistance, Figure 6a,b, respectively, are probed with a readout voltage of V_{read} = 0.5 V (lower than threshold voltage). Most of the grains reveal almost no currents in the initial state, with only a few exceptions at occasional grain boundaries marked by blue arrows in Figure 6b. The mean current for grain G1, for example, is therefore slightly elevated but still very low (<1 nA). Subsequently, the area was set into a low resistive state with a voltage of V_{SET} = 1.5 V. The readout in Figure 6c reveals an enhanced conductivity specifically for all marked grains, but not the whole scan area in accordance with Figure 3e. In particular, the grain boundaries exhibit the highest currents, marked with white and pink arrows in Figure 6c. The highest mean current is measured for grain G4 in the LRS, compare Figure 6e, since here the current is uniformly derived from the whole grain area. This validates that switching is preferred along the grain boundaries even for highly oxygen deficient hafnium oxide, like observed in Figure 4.

Subsequently, the now conductive grains were switched back into the HRS with a RESET voltage of V_{RESET} = −1.5 V. The successive readout in the current map in Figure 6d shows the reduced conductivity. Again, the conductivity remains highest along the grain boundaries. Nevertheless, there is an apparent difference between the grains G1 to G3 and the grains G4 to G6 in Figure 6. While no currents can be detected after RESET for the grains G4 to G6, an elevated current can still be observed for the grains G1 to G3, where the remaining current is mainly detected at the grain boundaries. This difference between the grains in Figure 6c,d implicates a dependence between the initial resistance and the resistance state after switching. The grain boundary of grain G1, marked by the white arrow in Figure 6c, has already a higher conductivity in the initial state, compare blue arrow to grain G1 in Figure 6a,b. Investigations on the switching kinetics of HfO_2-based devices showed that the SET and RESET voltage during a switching cycle depends strongly on the starting resistance and on the corresponding voltage of the previous cycle.[48,49] The switching voltage is therefore dependent on the resistance defined by the last cycle. This is in good agreement with the change in resistance of the grains shown in Figure 6.

Extracting the ON/OFF conductance ratio for the marked grains between the LRS and HRS, grains G1 to G3 have lower ratios than G4 to G6. Grain G4 has the highest ON/OFF ratio of about 43.7. Grains G1 and G2 have the lowest ratios of about 3.2 and 1.9, respectively. The current map in Figure 6c shows that the current of grain G4 is much more uniform than that of grains G1 and G2. With the smaller size of grain G1 the proportion of the grain boundary, which is identified as the main location for switching, is increased and hence leads to a larger ON/OFF conductance ratio. Therefore, the growth of smaller grains might enhance the ON/OFF conductance ratio and the uniformity of the conductance throughout the grain areas as one key variable of resistive switching.

Equivalent to the resistive switching of Hf(1.2), also Hf(0.9) grains could be switched with slightly higher SET/RESET voltage of ±1.8 V (not shown). The dominant rhombohedral phase facilitates resistive switching at lower biases in comparison to the monoclinic phase (see also Figure 5b,d). For samples with further reduced oxygen stoichiometry, the lack of an oxygen reservoir leads to a permanent failure in the ON state. For grains of the samples Hf(0.7) to Hf(0.1) no switching could be observed so far, while scanning a sample area with an increased voltage.

During the dielectric breakdown sporadic grains could only be switched irreversibly into a lower resistive state so far.

3. Conclusion

Hafnium oxide thin films with increasing oxygen deficiency were grown by MBE on TiN/Al_2O_3. In the stoichiometry range from HfO_2 to $HfO_{1.7}$ the phase transition from monoclinic to rhombohedral hafnium oxide was detected. While the phases exhibit no influence on the topography, the local electrical properties are significantly affected. The conductivity onset observed on the four most deficient samples varied between around 0.8 V for Hf(0.9) and 4.0 V for Hf(0.5). Thereby, current is initially detected at the grain boundaries regardless of the level of oxygen deficiency. With increasing SET voltage the highly conductive areas expand further. The conductivity of the various thin film samples decreases systematically with decreasing oxygen deficiency.

Likewise to the conductivity, also the forming voltage of single grains with mean diameter of around 27 nm scales with the level of oxygen deficiency. Grains of the monoclinic HfO_2 sample revealed the highest forming voltage at (7.0 ± 0.6) V. For $HfO_{1.7}$, the sample with the highest quantity of rhombohedral phase, grains have a significantly reduced forming voltage of (1.9 ± 0.8) V. While the overall conductivity scales with the level of oxygen deficiency, the grain boundaries reveal the highest conductivity for all investigated samples.

For the two highest oxygen deficient samples, resistive switching was observed on single grains. The initial resistance of the grains showed a significant impact on the latter resistance states after switching. While this investigation focuses on the physical understanding of switching in exemplary oxygen deficient HfO_{2-x} thin films, the behavior matches the observations of the switching kinetics in HfO_2-based devices, where the SET/RESET voltage can be altered by the previous cycle. The strongest resistance changes in the c-AFM measurements were detected along the grain boundaries. Small grains with uniform current revealed the best ON/OFF conductance ratios, which were more than 20× higher than larger grains with randomly distributed current. By decreasing the size of grains and increasing the relative amount of grain boundaries resistive switching properties could be enhanced even in smaller devices.

4. Experimental Section

Molecular Beam Epitaxy: All samples were grown using a custom designed MBE system at TU Darmstadt with a base pressure within the 10^{-9} mbar range. The metallic evaporation rates of hafnium (for hafnium oxide) and titanium (for titanium nitride) were controlled via quartz crystal microbalance (QCM) monitoring. The flow rates of oxygen and nitrogen had been regulated through designated mass flow controllers, respectively.

Prior deposition of hafnium oxide, the growth of epitaxial TiN was facilitated onto c-cut Al_2O_3 substrates. By extensive X-ray reflectometry (XRR) calibration uniform film thicknesses close to 34 nm for TiN had been achieved throughout the series. For this purpose, the growth conditions had been optimized to a titanium evaporation rate of 0.3 $Å s^{-1}$, while maintaining a nitrogen flow of 0.6 standard cubic centimeters per minute (sccm). To promote the reactivity of nitrogen, it was exited into a plasma with a radio frequency (RF) power of 340 W. During TiN deposition a constant Al_2O_3 substrate temperature of 800 °C was achieved via thermocouple-calibrated resistive heating. The successful growth of utmost epitaxial TiN was confirmed by the prominent Laue oscillations on both sides of the (111) TiN reflection in the XRD scans in Figure 1b, indicating highly crystalline growth with strongly coherent lattice planes. Further, close-to-stoichiometric conditions were indicated by the (111) TiN reflex position, which was close to the value of bulk TiN (PDF 00-038-1420). Note that this reflection developed a small shoulder toward higher angles. This was likely a result of the deposition route, where for the first view layers higher Ti evaporation rates close to 0.9 $Å s^{-1}$ were chosen in order to reduce the interfacial strain between TiN and Al_2O_3.

For the deposition of all HfO_{2-x} thin films, a constant TiN/Al_2O_3 substrate temperature of 320 °C was set. The RF power was held constant at 200 W for the corresponding oxygen plasma excitation. By XRR calibration uniform HfO_{2-x} film thicknesses of 10 nm were achieved.

In order to strictly avoid critical oxidation of oxygen deficient hafnium oxide, all thin films had been stored in ultra-high vacuum conditions immediately after synthesis. Therefore, the samples were transported in vacuo from the MBE system to the SPM at Forschungszentrum Jülich GmbH by the use of a custom designed vacuum suitcase by Mantis Deposition Ltd. (Birmingham, UK).

X-Ray Diffraction and Reflectometry: XRD and XRR measurements had been carried out with a Rigaku SmartLab four-axis goniometer with rotating Cu anode. All samples had been characterized in parallel beam configuration, using a Ge(220) double-bounce monochromator employing Cu $K\alpha_1$ radiation. Prior $2\theta/\omega$ XRD measurements, all samples had been aligned to the (006) out of plane reflection of the Al_2O_3 substrate (see Figure S1, Supporting Information). For thickness calibration, XRR data had been fitted using a two-layer model of $HfO_{2-x}/TiN/Al_2O_3$ within XRR RefSim.[50]

Conductive Atomic Force Microscopy: All c-AFM investigations were performed at Forschungszentrum Jülich GmbH with a commercial VT-SPM (Scienta Omicron GmbH, Taunusstein, Germany) at room temperature with a base pressure below 1×10^{-9} mbar. The tip bias, which was applied with respect to the TiN-layer, can be varied between ± 10 V, while the maximum detectable absolute current was 333 nA. The normal force between cantilever and sample surface was set to 1 nN. Two different kinds of cantilevers were used, either PtIr-coated Si-cantilevers with tip radius <25 nm (PPP-CONTPt, Nanosensors, Neuchatel, Switzerland), or conductive single crystal diamond probes with tip radius <5 nm (AD-2.8-SS, Bruker AFM Probes, Wissembourg, France). The latter was used for all resistive switching measurements, while the PtIr-cantilever was utilized for all other c-AFM scans. The contact resistance of the cantilevers was tested on an Au single crystal and only cantilevers that showed currents about $I \approx 250$ nA with applied bias of $V_{set} = 5$ mV were used. Shown c-AFM images were processed under the use of common filter methods with MountainsSPIP software (Version 9.1, Digital Surf, Besancon, France). The height scales of all topography maps were given relative to the center of the mean plane of the image.

Supporting Information

Supporting Information is available from the Wiley Online Library or from the author.

Acknowledgements

This work was financially supported by the Deutsche Forschungsgemeinschaft (DFG) through SFB 917 "Nanoswitches" and the Leibniz Prize 2014 of the DFG to Rainer Waser (WA 908/30-1). Furthermore, the work leading to this publication had also been undertaken in the framework of the projects WAKeMeUP and StorAIge, which received funding from the Electronic Components and Systems for European Leadership Joint Undertaking in collaboration with the European Union's H2020 Framework Programme (H2020/2014-2020) and National Authorities, under grant agreement no. 783176 and no. 101007321, respectively. Funding

by the Federal Ministry of Education and Research (BMBF) under contract 16ESE0298 and 16MEE0154, respectively, is gratefully acknowledged. This work was supported by the Deutsche Forschungsgemeinschaft under project 384682067, AL 560/21-1.

Open access funding enabled and organized by Projekt DEAL.

Conflict of Interest

The authors declare no conflict of interest.

Author Contributions

R.D., S.K., R.W., and L.A. planned the experiments. N.K., T.V., and E.P. performed MBE and XRD experiments. N.S. executed AFM experiments and all analyses. N.S. and N.K. wrote the manuscript with contributions of all authors. All authors have given approval to the final version of the manuscript.

Data Availability Statement

The data that support the findings of this study are available from the corresponding author upon reasonable request.

Keywords

c-AFM, defect engineering, grain boundaries, hafnium oxide, MBE, resistive switching

Received: October 9, 2023
Revised: December 22, 2023
Published online: January 17, 2024

[1] R. Dittmann, J. P. Strachan, *APL Mater.* **2019**, *7*, 11.
[2] M.-K. Song, J.-H. Kang, X. Zhang, W. Ji, A. Ascoli, I. Messaris, A. S. Demirkol, B. Dong, S. Aggarwal, W. Wan, S.-M. Hong, S. G. Cardwell, I. Boybat, J. sun Seo, J.-S. Lee, M. Lanza, H. Yeon, M. Onen, J. Li, B. Yildiz, J. A. del Alamo, S. Kim, S. Choi, G. Milano, C. Ricciardi, L. Alff, Y. Chai, Z. Wang, H. Bhaskaran, M. C. Hersam, et al., *ACS Nano* **2023**, *17*, 11994.
[3] D. Ielmini, H.-S. P. Wong, *Nat. Electron.* **2018**, *1*, 333.
[4] S. U. Sharath, S. Vogel, L. Molina-Luna, E. Hildebrandt, C. Wenger, J. Kurian, M. Duerrschnabel, T. Niermann, G. Niu, P. Calka, M. Lehmann, H.-J. Kleebe, T. Schroeder, L. Alff, *Adv. Funct. Mater.* **2017**, *27*, 1700432.
[5] R. Winkler, A. Zintler, S. Petzold, E. Piros, N. Kaiser, T. Vogel, D. Nasiou, K. P. McKenna, L. Molina-Luna, L. Alff, *Adv. Sci.* **2022**, *9*, 2201806.
[6] N. Kaiser, T. Vogel, A. Zintler, S. Petzold, A. Arzumanov, E. Piros, R. Eilhardt, L. Molina-Luna, L. Alff, *ACS Appl. Mater. Interfaces* **2021**, *14*, 1290.
[7] N. Schmidt, K. Z. Rushchanskii, U. Trstenjak, R. Dittmann, S. Karthäuser, *ACS Appl. Nano Mater.* **2023**, *6*, 148.
[8] M. P. Mueller, F. Gunkel, S. Hoffmann-Eifert, R. A. D. Souza, *J. Appl. Phys.* **2021**, *129*, 025104.
[9] D. Duncan, B. Magyari-Köpe, Y. Nishi, *Appl. Phys. Lett.* **2016**, *108*, 043501.
[10] Y. Wang, G. Niu, Q. Wang, S. Roy, L. Dai, H. Wu, Y. Sun, S. Song, Z. Song, Y.-H. Xie, Z.-G. Ye, X. Meng, W. Ren, *Nanotechnology* **2020**, *31*, 205203.
[11] K. Z. Rushchanskii, S. Blügel, M. Ležaić, *Faraday Discuss.* **2019**, *213*, 321.
[12] D.-Y. Cho, H. S. Jung, I.-H. Yu, J. H. Yoon, H. K. Kim, S. Y. Lee, S. H. Jeon, S. Han, J. H. Kim, T. J. Park, B.-G. Park, C. S. Hwang, *Chem. Mater.* **2012**, *24*, 3534.
[13] B. Govoreanu, G. Kar, Y.-Y. Chen, V. Paraschiv, S. Kubicek, A. Fantini, I. Radu, L. Goux, S. Clima, R. Degraeve, N. Jossart, O. Richard, T. Vandeweyer, K. Seo, P. Hendrickx, G. Pourtois, H. Bender, L. Altimime, D. Wouters, J. Kittl, M. Jurczak, in *2011 International Electron Devices Meeting*, IEEE, Piscataway, NJ **2011**, pp. 31.6.1–31.6.4.
[14] K. Z. Rushchanskii, S. Blügel, M. Ležaić, *Phys. Rev. Mater.* **2018**, *2*, 115002.
[15] S. M. Aspera, H. Kasai, H. Kishi, N. Awaya, S. Ohnishi, Y. Tamai, *J. Electron. Mater.* **2012**, *42*, 143.
[16] G.-Q. Mao, K.-H. Xue, Y.-Q. Song, W. Wu, J.-H. Yuan, L.-H. Li, H. Sun, S. Long, X.-S. Miao, *AIP Adv.* **2019**, *9*, 105007.
[17] Y. Yang, X. Zhang, L. Qin, Q. Zeng, X. Qiu, R. Huang, *Nat. Commun.* **2017**, *8*, 1.
[18] C. Li, B. Gao, Y. Yao, X. Guan, X. Shen, Y. Wang, P. Huang, L. Liu, X. Liu, J. Li, C. Gu, J. Kang, R. Yu, *Adv. Mater.* **2017**, *29*, 1602976.
[19] Y. Zhang, G.-Q. Mao, X. Zhao, Y. Li, M. Zhang, Z. Wu, W. Wu, H. Sun, Y. Guo, L. Wang, X. Zhang, Q. Liu, H. Lv, K.-H. Xue, G. Xu, X. Miao, S. Long, M. Liu, *Nat. Commun.* **2021**, *12*, 1.
[20] K. Skaja, M. Andrä, V. Rana, R. Waser, R. Dittmann, C. Baeumer, *Sci. Rep.* **2018**, *8*, 1.
[21] K. P. McKenna, *Modell. Simul. Mater. Sci. Eng.* **2014**, *22*, 025001.
[22] S. U. Sharath, T. Bertaud, J. Kurian, E. Hildebrandt, C. Walczyk, P. Calka, P. Zaumseil, M. Sowinska, D. Walczyk, A. Gloskovskii, T. Schroeder, L. Alff, *Appl. Phys. Lett.* **2014**, *104*, 063502.
[23] S. Lee, D. Lee, J. Woo, E. Cha, J. Park, J. Song, K. Moon, Y. Koo, B. Attari, N. Tamanna, M. S. Haque, H. Hwang, *IEEE Electron Device Lett.* **2013**, *34*, 1515.
[24] K.-H. Xue, P. Blaise, L. R. C. Fonseca, G. Molas, E. Vianello, B. Traoré, B. D. Salvo, G. Ghibaudo, Y. Nishi, *Appl. Phys. Lett.* **2013**, *102*, 201908.
[25] L. Vandelli, A. Padovani, L. Larcher, G. Bersuker, *IEEE Trans. Electron Devices* **2013**, *60*, 1754.
[26] K. McKenna, A. Shluger, V. Iglesias, M. Porti, M. Nafría, M. Lanza, G. Bersuker, *Microelectron. Eng.* **2011**, *88*, 1272.
[27] M. Lanza, K. Zhang, M. Porti, M. Nafría, Z. Y. Shen, L. F. Liu, J. F. Kang, D. Gilmer, G. Bersuker, *Appl. Phys. Lett.* **2012**, *100*, 123508.
[28] M. Lanza, G. Bersuker, M. Porti, E. Miranda, M. Nafría, X. Aymerich, *Appl. Phys. Lett.* **2012**, *101*, 193502.
[29] S. Brivio, G. Tallarida, E. Cianci, S. Spiga, *Nanotechnology* **2014**, *25*, 385705.
[30] S. Petzold, A. Zintler, R. Eilhardt, E. Piros, N. Kaiser, S. U. Sharath, T. Vogel, M. Major, K. P. McKenna, L. Molina-Luna, L. Alff, *Adv. Electron. Mater.* **2019**, *5*, 1900484.
[31] K. Szot, W. Speier, G. Bihlmayer, R. Waser, *Nat. Mater.* **2006**, *5*, 312.
[32] R. Muenstermann, J. J. Yang, J. P. Strachan, G. Medeiros-Ribeiro, R. Dittmann, R. Waser, *Physica Status Solidi (RRL) - Rapid Res. Lett.* **2009**, *4*, 16.
[33] R. Muenstermann, T. Menke, R. Dittmann, S. Mi, C.-L. Jia, D. Park, J. Mayer, *J. Appl. Phys.* **2010**, *108*, 124504.
[34] R. Muenstermann, T. Menke, R. Dittmann, R. Waser, *Adv. Mater.* **2010**, *22*, 4819.
[35] R. Dittmann, R. Muenstermann, I. Krug, D. Park, T. Menke, J. Mayer, A. Besmehn, F. Kronast, C. M. Schneider, R. Waser, *Proc. IEEE* **2012**, *100*, 1979.
[36] J. Y. Son, Y.-H. Shin, *Appl. Phys. Lett.* **2008**, *92*, 222106.
[37] S. Kremmer, H. Wurmbauer, C. Teichert, G. Tallarida, S. Spiga, C. Wiemer, M. Fanciulli, *J. Appl. Phys.* **2005**, *97*, 074315.

[38] U. Celano, L. Goux, R. Degraeve, A. Fantini, O. Richard, H. Bender, M. Jurczak, W. Vandervorst, *Nano Lett.* **2015**, *15*, 7970.
[39] U. Celano, A. Fantini, R. Degraeve, M. Jurczak, L. Goux, W. Vandervorst, *AIP Adv.* **2016**, *6*, 085009.
[40] N. Kaiser, Y.-J. Song, T. Vogel, E. Piros, T. Kim, P. Schreyer, S. Petzold, R. Valentí, L. Alff, *ACS Appl. Electron. Mater.* **2023**, *5*, 754.
[41] F. Zahoor, T. Z. A. Zulkifli, F. A. Khanday, *Nanoscale Res. Lett.* **2020**, *15*, 1.
[42] J. Wang, H. P. Li, R. Stevens, *J. Mater. Sci.* **1992**, *27*, 5397.
[43] E. Hildebrandt, J. Kurian, L. Alff, *J. Appl. Phys.* **2012**, *112*, 11.
[44] E. Piros, M. Lonsky, S. Petzold, A. Zintler, S. Sharath, T. Vogel, N. Kaiser, R. Eilhardt, L. Molina-Luna, C. Wenger, J. Müller, L. Alff, *Phys. Rev. Appl.* **2020**, *14*, 034029.
[45] O. Pirrotta, L. Larcher, M. Lanza, A. Padovani, M. Porti, M. Nafría, G. Bersuker, *J. Appl. Phys.* **2013**, *114*, 134503.
[46] V. Iglesias, M. Lanza, K. Zhang, A. Bayerl, M. Porti, M. Nafría, X. Aymerich, G. Benstetter, Z. Y. Shen, G. Bersuker, *Appl. Phys. Lett.* **2011**, *99*, 103510.
[47] M. Moors, K. K. Adepalli, Q. Lu, A. Wedig, C. Bäumer, K. Skaja, B. Arndt, H. L. Tuller, R. Dittmann, R. Waser, B. Yildiz, I. Valov, *ACS Nano* **2016**, *10*, 1481.
[48] F. Cüppers, S. Menzel, C. Bengel, A. Hardtdegen, M. von Witzleben, U. Böttger, R. Waser, S. Hoffmann-Eifert, *APL Mater.* **2019**, *7*, 091105.
[49] T. Diokh, E. Le-Roux, S. Jeannot, M. Gros-Jean, P. Candelier, J. F. Nodin, V. Jousseaume, L. Perniola, H. Grampeix, T. Cabout, E. Jalaguier, M. Guillermet, B. D. Salvo, in *2013 IEEE International Reliability Physics Symposium (IRPS)*, IEEE, Piscataway, NJ **2013**, pp. 5E.4.1–5E.4.4.
[50] P. Zaumseil, *RCRefSim (Rocking Curve and Reflectivity Simulation)*, IHP Frankfurt (Oder), Germany **2005**.